

# Fast multifrequency measurement of nonlinear conductance

Riccardo Borgani,<sup>1,\*</sup> Mojtaba Gilzad Kohan,<sup>2</sup> Alberto Vomiero,<sup>2</sup> and David B. Haviland<sup>1</sup>

<sup>1</sup>*Nanostructure Physics, KTH Royal Institute of Technology, 10691 Stockholm, Sweden*

<sup>2</sup>*Department of Engineering Sciences and Mathematics,  
Luleå University of Technology, 97187 Luleå, Sweden*

(Dated: May 15, 2022)

**Low noise measurement of small currents in nanometer-scale junctions is of central importance to the characterization of novel high-performance devices and materials<sup>1–3</sup> for applications ranging from energy harvesting and energy conversion<sup>4–8</sup> to topological materials for quantum computers<sup>9,10</sup>.** The high resistance of these junctions and the stray capacitance of their measurement leads impose speed limitations (tens of seconds) on the traditional methods of measuring their nonlinear conductance, making detailed investigations of change with external fields or maps of variation over a surface impractical, if not impossible. Here we demonstrate fast (milliseconds) reconstruction of nonlinear current-voltage characteristics from phase-coherent multifrequency lock-in data using the inverse Fourier transform. The measurement technique allows for separation of the galvanic and displacement currents in the junction and easy cancellation of parasitic displacement current due to the measurement leads. We use the method to reveal nanometer-scale variations in the electrical transport properties of organic photovoltaic and semiconducting thin films. The method has broad applicability and its wide-spread implementation promises advancement in high-speed and high-resolution characterization for nanotechnology.

To probe physical phenomena at the nanometer scale we must extract a weak signal from a small volume and bring it into the macroscopic world of laboratory measurement instruments. This change of scale introduces limitations on the speed of measurement because our instruments must average in order to reduce the random noise in relation to the weak deterministic signal. The connections between the instruments and the nanometer scale device also introduce parasitic effects that further limit speed. For example, the capacitance of electrical leads introduces a parallel displacement current that can easily be much larger than the galvanic current flowing through a nanometer scale junction, causing the amplifier to saturate and thereby limit its gain. In this paper we show how to overcome these speed limitations by canceling the large linear response due to the parallel displacement current, to extract the much smaller galvanic current and rapidly measure its nonlinear character by multiplexing in the frequency domain.

Coherent frequency-domain multiplexing and its associated increase in the speed of measurement allows for

removing 1/f noise and instrument drift when investigating how nonlinear conductance changes with external parameters such as gate voltage, magnetic field or location on a surface. This feature is particularly useful in scanning tunneling microscopy<sup>11</sup> (STM) and conductive atomic force microscopy<sup>12</sup> (AFM), where slow measurement results in two basic modes of operation. In imaging mode current is measured while scanning the surface with a constant tip-sample bias, quickly generating an image with only limited information about the electrical properties of the sample, *i.e.* the current at one voltage bias. Multiple successive scans at different applied bias are required to get the full current-voltage characteristic (IVC), causing problems due to tip wear and instrument drift during the long measurement time. In spectroscopic mode the IVC is recorded at fixed tip position where the sample bias is slowly swept. Lateral resolution is achieved by performing the bias sweep at a grid of specified tip positions, greatly reducing the speed of the scan. Here we demonstrate spectroscopic mode while scanning at the speed of imaging mode.

We demonstrate the method on conductive AFM, but it is quite general and could easily be adapted for rapid exploration of the gate-voltage or magnetic field dependence of IVCs in quantum devices. Recent efforts with conductive AFM<sup>13</sup> have used high-speed acquisition of data while scanning at imaging speeds to extract IVCs from large time-domain data sets (gigabytes per scan) using complicated and computationally expensive filtering based on statistical inference that requires several hours of analysis<sup>14</sup>. In contrast, we take a deterministic approach that exploits our knowledge of the periodic drive signal and does not require any assumptions about the functional form of the nonlinear IVC or the bias dependence of the junction capacitance. The method efficiently rejects noise and it compresses the three-dimensional data set to a manageable size for storage. Using the inverse Fast Fourier Transform (iFFT), analysis is computationally efficient and easily performed in real-time on a notebook computer – an extremely valuable feature for the experimentalist who needs instantaneous feedback for adjusting measurement conditions.

## I. THEORY

Figure 1 shows a schematic representation of the measurement setup, defining the relevant electrical quantities. When a time-dependent bias  $V(t)$  is applied be-

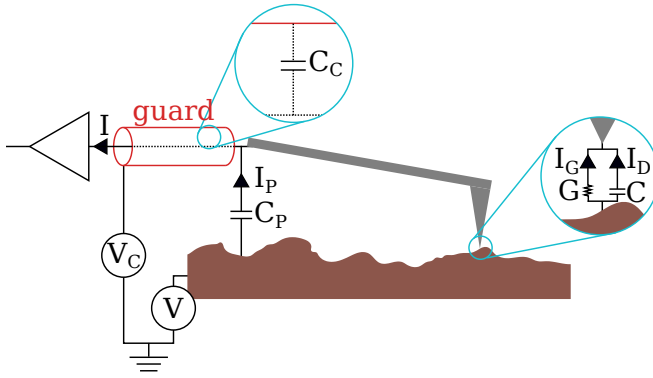


FIG. 1. **Experimental setup and electrical connections.** Not to scale. The conductance  $G$  and the capacitance  $C$  model the tip-sample contact,  $C_P$  is the parasitic capacitance,  $C_C$  the capacitance of the coaxial cable (guard).  $V$  is the tip-sample bias voltage, and  $V_C$  is the compensation drive to the shield of the coaxial cable.  $I$  is the total current at the input of the trans-impedance amplifier.

tween the AFM tip and a conductive sample, the total current through the tip is

$$I = I_G + I_D + I_P = G(V)V + C(V)\dot{V} + C_P\dot{V}. \quad (1)$$

We call the three terms  $I_G$ ,  $I_D$  and  $I_P$  the galvanic, displacement and parasitic current, respectively. The bias and its time derivative  $\dot{V}$  are known experimental signals. The parallel conductance  $G$  and capacitance  $C$  model the junction between the tip and the sample. We emphasize that both the conductance  $G(V)$  and the capacitance  $C(V)$  can be nonlinear functions of  $V$ , in contrast to other techniques<sup>13</sup> which assume that the capacitance is independent of voltage.  $C_P$  is a distributed parasitic capacitance in parallel with the junction, modeling the capacitive contributions of the probe holder, the cables, and the rest of the measuring electronics.

Good electrical design with proper guarding can minimize  $C_P$ . However, at the highest gains necessary to measure current in the sub-picoampere range, the parasitic displacement current  $I_P = C_P\dot{V}$  due to a residual un-guarded  $C_P$  can easily saturate the trans-impedance amplifier. We therefore utilize a compensation technique where we apply an appropriate compensation voltage  $V_C(t)$  to the guard so as to nullify  $I_P$  (see Methods section).

To measure the remaining galvanic and displacement currents, we apply a time-dependent sample bias of the form  $V(t) = V_{AC} \cos(\omega_1 t)$ . Assuming  $G(V)$  and  $C(V)$  are analytic functions,  $I_G(t)$  and  $I_D(t)$  share the same time periodicity as  $V$  and can therefore be written as a Fourier series (see also Methods section):

$$I_G(t) = \sum_{k=0}^{+\infty} I_{Gk} \cos(k\omega_1 t), \quad (2)$$

$$I_D(t) = \sum_{k=0}^{+\infty} I_{Dk} \sin(k\omega_1 t), \quad (3)$$

where the  $\{I_{Gk}\}$  and  $\{I_{Dk}\}$  are real constants. Equations (2) and (3) show that the two current contributions are easily distinguishable: the galvanic current is in phase with  $V$ , and the displacement current is in phase with  $\dot{V}$ . We can therefore obtain the galvanic and displacement currents from the real and imaginary part, respectively, of the Fourier Transform of the measured compensated current:

$$\hat{I}_G(\omega) = \Re[\hat{I}(\omega)], \quad (4)$$

$$\hat{I}_D(\omega) = i\Im[\hat{I}(\omega)]. \quad (5)$$

Once the separate  $\hat{I}_G(\omega)$  and  $\hat{I}_D(\omega)$  are obtained, we use the inverse Fourier transform to get  $I_G(t)$  and  $I_D(t)$  (Fig. 2b and 2e). We finally plot  $I_G(t)$  versus the applied  $V(t)$  to obtain the IVC, free of any capacitive contribution (Fig. 2c and 2f). Alternatively, we could plot the differential conductance  $\partial I_G / \partial V = \dot{I}_G / \dot{V}$  versus  $V$ , where the time derivatives are easily found in the frequency domain by multiplication with  $i\omega$ .

Similarly we can plot the junction capacitance  $C = I_D / \dot{V}$  versus  $V$ , which can give insight to the junction area and dielectric properties of the material surface (Fig. 2c and 2f). Note that this capacitance is ideally that of the junction itself as the parasitic capacitance is removed when compensating for  $I_P$  (see Methods section). However, some residual parallel capacitance local to the tip may be present, depending on the quality of the compensation.

The Fourier components of the current  $\{\hat{I}_k\}$  are measured simultaneously (Fig. 2a) with a multifrequency lock-in amplifier and the quadrature data received from the lock-in is processed on a computer to reconstruct  $I_G(t)$  and  $I_D(t)$ . A key point here is that the lock-in frequencies and measurement bandwidth must be properly tuned to the sample bias frequency  $\omega_1$  (the reference oscillation). The nonlinear information of the IVC is then coded in the harmonics, or integer multiples of  $\omega_1$ . When  $N$  harmonics are measured in a given time (inverse bandwidth) a factor  $N$  improvement of measurement speed is achieved at the same signal-to-noise ratio, in comparison to traditional methods that sweep voltage and measure current in the time domain.

## II. EXPERIMENTAL RESULTS

We demonstrate the technique on an organic solar cell consisting of a TQ1:T10 polymer blend on a PEDOT:PSS/PEI transparent electrode. The AFM is mounted on an inverted optical microscope, the objective of which is used to focus the light from a white light-emitting diode (LED) onto a small spot around the area scanned. The LED illumination is alternately switched on and off during the scanning trace and retrace in order to compare the electrical response of the material under light and dark conditions.

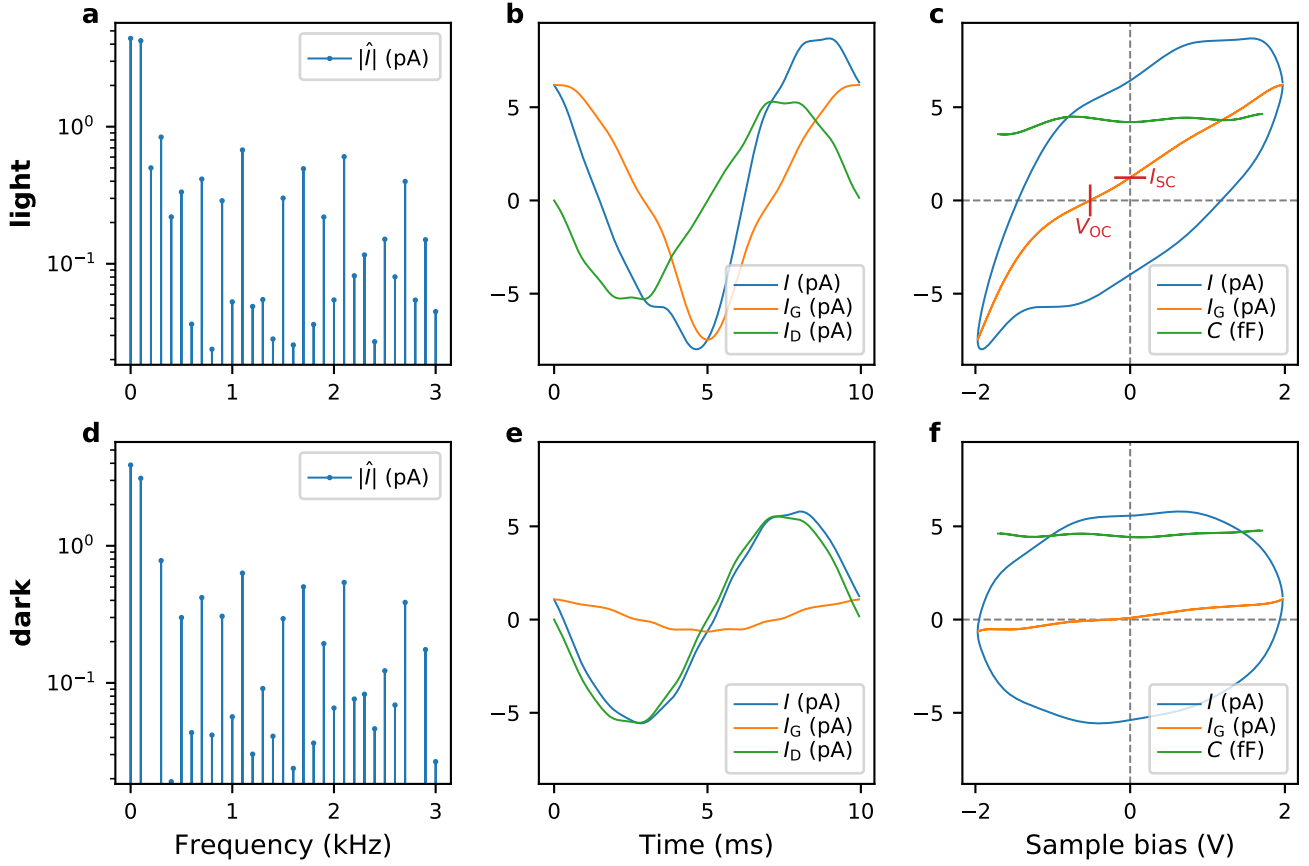


FIG. 2. **Current-voltage characteristics on a photo-active polymer blend.** Measurement under light (a-c) and dark (d-f) conditions. a and d, amplitude of the measured current at 31 frequencies, the phase is also measured but not shown. b and e, total, galvanic and displacement currents as a function of time obtained from the current spectrum by inverse Fourier transform of Eq.s (4) and (5). c and f, reconstructed currents and junction capacitance vs. voltage. The loop in the total current  $I(V)$  is due to the junction capacitance. The galvanic current  $I_G(V)$  does not show such a loop. The junction capacitance  $C$  is nearly constant, as expected.

Figure 2a shows the amplitude of the measured current spectrum  $|\hat{I}(\omega)|$  and 31 harmonics of the sample bias frequency  $\omega_1$ . The two spectra are acquired at the same spot on the sample, under light (trace) and dark (retrace) conditions. Using the inverse Fourier transform we plot the galvanic and displacement current components in Fig. 2b and 2e for light and dark respectively, where one can see that the displacement current does not change significantly with illumination. On the other hand, the galvanic current increases dramatically when the light is turned on.

These differences are clear in the reconstructed IVCs in Fig. 2c and 2f. Under illumination the material presents a typical photo-diode response, with an offset current at zero applied voltage (short-circuit current  $I_{SC}$ ) and a finite voltage required to obtain zero current (open-circuit voltage  $V_{OC}$ ). In dark, only a residual resistive contribution is visible.

The spectra, and therefore the IVCs, of Fig. 2 are obtained at every pixel while scanning at normal speed for

contact mode. Rates of 1000 pixels/sec are easily accessible, yielding a trace-retrace image with 256x256 pixels resolution (130,000 IVCs, file size 35 MB) in about 2 minutes, or under 9 minutes for 512x512 resolution (over 520,000 IVCs, file size 170 MB). To date, this is the fastest and most optimally compressed method for measuring and storing IVCs.

Having the full IVC at every pixel allows for the mapping of interesting electrical properties of the material with very high resolution. Figure 3 shows the reconstructed values of  $I_{SC}$ ,  $V_{OC}$  and the current  $I_{RV}$  measured at a reverse bias of 1 V. Due to the computational efficiency of the iFFT, the analysis of the entire scan takes less than one second on a notebook computer and can therefore be performed in real time, while scanning with the AFM.

We analyze another sample consisting of a copper oxide  $\text{CuO}_2$  / zinc oxide  $\text{ZnO}$  thin-film p/n junction deposited on a fluorine-doped tin oxide (FTO) conducting glass. Such composite oxide materials find application

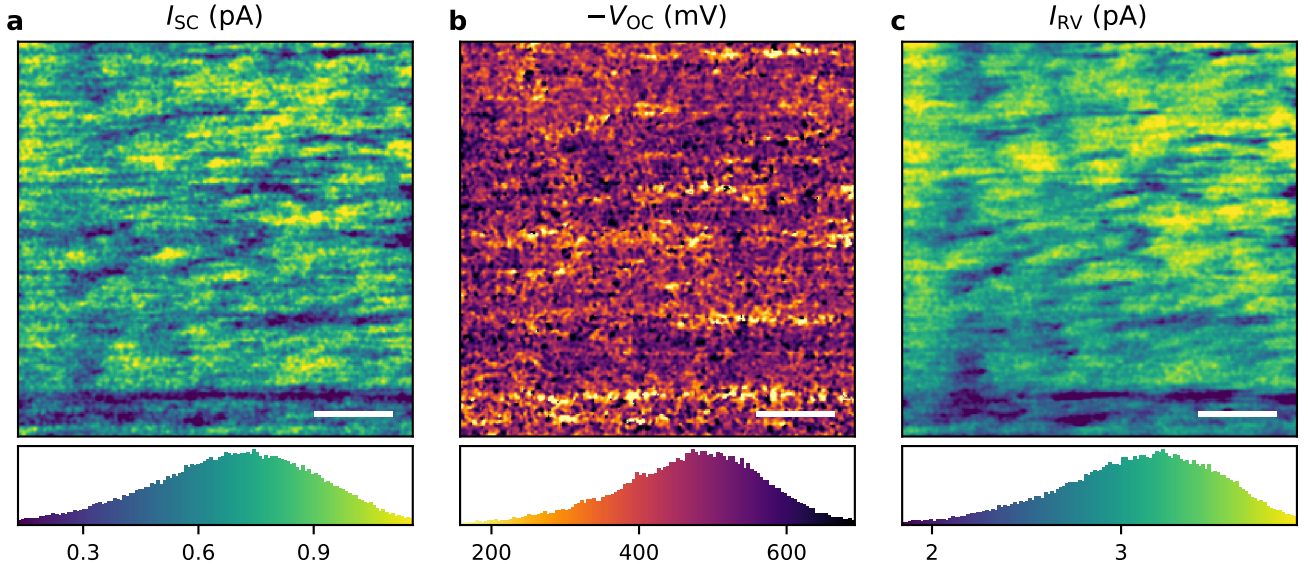


FIG. 3. **Parameter maps on a photo-active polymer blend.** Maps and histograms of: **a**, short-circuit current  $I_{SC}$ ; **b**, open-circuit voltage  $V_{OC}$ ; **c**, reverse-bias current  $I_{RV}$ . The white scale bars are 200 nm.

in sensing<sup>15</sup>, energy conversion<sup>16,17</sup> and lighting<sup>18</sup>, and their nanoscale characterization is needed for understanding their functionality. Figure 4a shows that the junction of the two semiconductors presents a typical diode-like IVC, with current flowing only for positive applied bias (orange curve). However, some areas of the sample show a symmetric IVC (blue curve) indicating a damage in the CuO<sub>2</sub> or a resistive phase of the composite material. Other areas show zero current in both bias directions (green curve), indicating bad contact between the tip and the sample or perhaps an insulating material phase.

To analyze the spatial distribution of these three classes of IVC, we plot the current  $I_+$  at fixed forward bias  $V_+ = 0.75$  V and the current  $I_-$  at fixed reversed bias  $V_- = -0.75$  V. In the forward bias image (Fig. 4b) both diode-like and resistor-like areas have high current and appear as bright spots, while areas with no current are dark. In the reverse bias image (Fig. 4c), the resistor-like areas stand out as bright spots while the diode-like and no-current areas remain dark. To highlight the diode-like areas, we analyze the symmetry properties of the acquired IVCs: resistor-like curves have a clear odd symmetry around zero (Fig. 4e), and regions with diode-like curves have a stronger even-symmetry component (Fig. 4d). The two images are combined using the symmetry parameter  $S$  in Fig. 4f (see detailed description in the Methods section).

### III. CONCLUSIONS

We described and demonstrated a new measurement paradigm for capturing nonlinear current-voltage characteristics from weak and noisy signals. Using one stable

reference oscillation for phase-sensitive detection of many harmonics, we achieved frequency-domain multiplexing of the information contained in the nonlinear IVC. Another important advantage of our frequency-domain approach is that we can easily extract the separate contributions of the galvanic and displacement currents in the measured total current. The frequency-domain data is an optimally compressed representation of the nonlinear response and it is computationally efficient to reconstruct the IVC using the iFFT algorithm. The frequency domain approach also provides for simple cancellation of the large parasitic current due to the stray capacitance of the leads, allowing for larger gain without saturation of the current amplifier. Together these advantages allow for greatly enhanced measurement speed, compact data storage, and real-time feedback while measuring.

We used scanning probe microscopy to demonstrate the power of the method, reconstructing the full IVC at every pixel of a conducting AFM image, without compromising the scanning speed. With the IVC at every pixel we constructed *a posteriori* images that highlight the interesting figures of merit for electric transport. With standard conductive AFM one would have to decide *a priori* what set of voltage biases to apply and then perform multiple scans of the same area at each bias, while fighting instrument drift and tip wear that make the scans difficult or impossible to correlate. The multifrequency approach provides a general solution to a very general and common problem in nanotechnology and its easy implementation has recently been made possible with the advent of tuned multifrequency digital lock-in amplifiers.

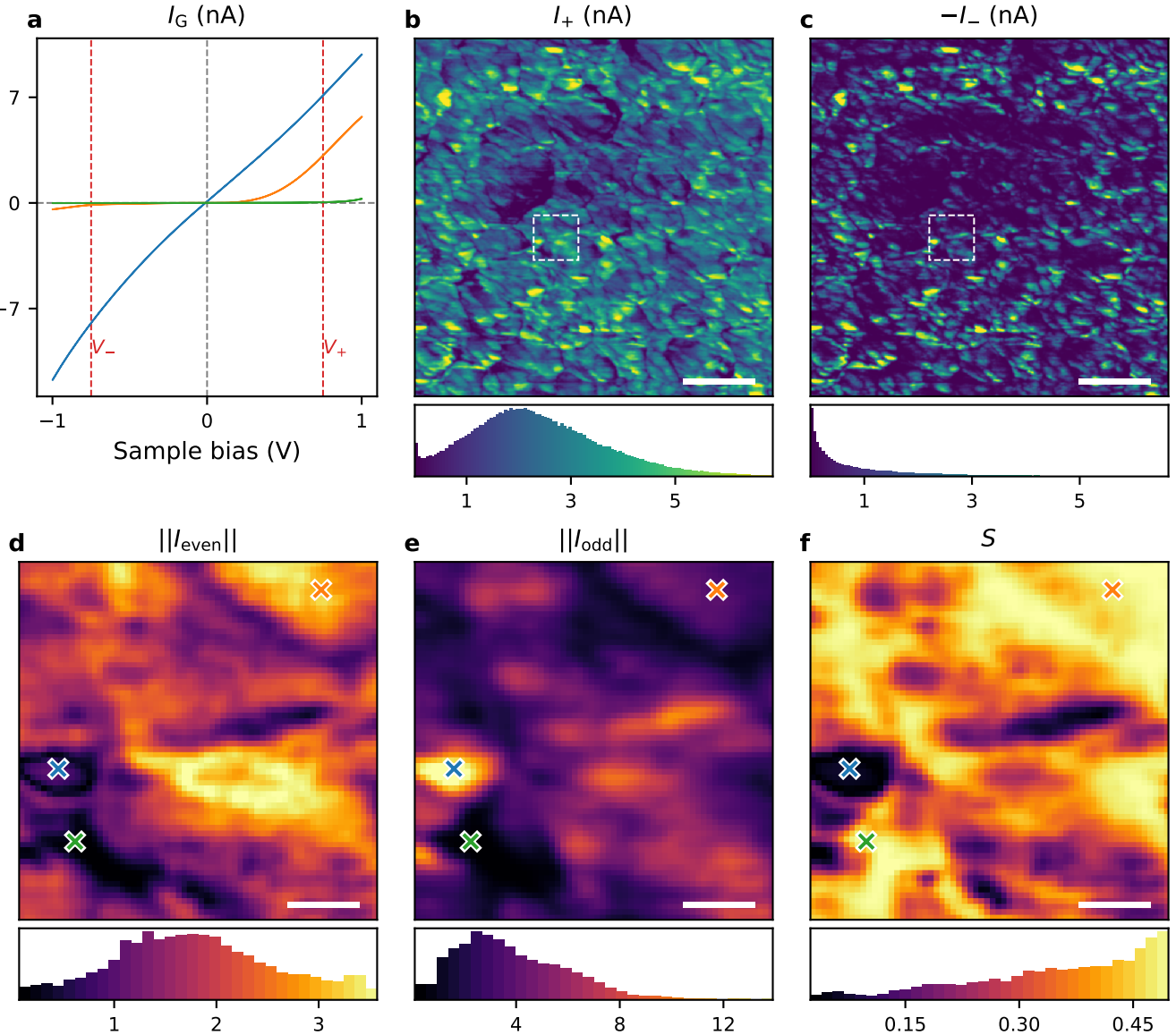


**FIG. 4. Measurements on a thin-film all-oxide p/n junction.** **a**, representative IVCs on different locations of the sample. Maps and histograms of: **b**, current  $I_+$  at forward bias  $V_+ = 0.75$  V; **c**, current  $I_-$  at reverse bias  $V_- = -0.75$  V; **d**, even-symmetry current  $||I_{\text{even}}||$ ; **e**, odd-symmetry current  $||I_{\text{odd}}||$ ; **f**, symmetry parameter  $S = ||I_{\text{even}}||/(||I_{\text{even}}|| + ||I_{\text{odd}}||)$ . The maps in **d**, **e** and **f** are on a zoomed area marked by the white dashed boxes in **b** and **c**. The white scale bars are 200 nm in **b** and **c**, and 25 nm in **d**, **e** and **f**. The crosses in **d**, **e** and **f** mark the positions where the IVCs of corresponding colors are acquired.

## ACKNOWLEDGMENTS

The authors acknowledge O. Inganäs and Y. Xia for providing the organic solar cell sample. DBH and RB acknowledge financial support from the Swedish Research Council (VR), and the Knut and Alice Wallenberg Foundation. AV and MGK acknowledge financial support from the Kempe Foundation and the Knut and Alice Wallenberg Foundation.

## Appendix: METHODS

### 1. Instrumentation

The current flowing through the AFM tip  $I$  is converted to voltage by a variable-gain low-noise current amplifier DLPCA-200 (FEMTO Messtechnik GmbH). The voltage is then sampled by a digital multifrequency lock-in amplifier (MLA, Intermodulation Products AB), and the real and imaginary part of 32 frequency components

$\{I_{Gk}\}$  and  $\{I_{Dk}\}$  are read via ethernet by a computer for analysis. Two output ports on the MLA are used to apply the sample bias  $V$  and the compensation voltage  $V_C$ . The measurement and analysis routines are implemented in the scripting interface of the MLA control software. They are written in Python and make use of the Fast Fourier Transform<sup>19</sup> and other routines in the SciPy and NumPy libraries<sup>20</sup>.

The measurements on the organic solar cell sample are performed on a NanoWizard ULTRA Speed AFM (JPK Instruments AG) mounted on an inverted optical microscope (Nikon Corporation). The measurements on the CuO<sub>2</sub>/ZnO sample are performed on a Dimension Icon AFM (Bruker Corporation). In both cases, the AFM is operated in contact mode with a RMN-12PT400B cantilever (Bruker, nominal spring constant 0.3 N/m).

## 2. Parasitic current compensation

We have previously shown how to compensate for parasitic forces in dynamic AFM<sup>21</sup>, a *passive* compensation in the sense that the parasitic forces are measured and subtracted from the data, but not counteracted during the measurement. To prevent a saturation of the trans-impedance amplifier it is necessary to use *active* compensation, where the parasitic current  $I_P$  is not only measured but also nullified before it reaches the amplifier.

With the tip lifted away from the sample surface (tens to hundreds of micrometers),  $I_G$  and  $I_C$  in Eq. (1) are both zero. Explicitly accounting for the capacitance  $C_C$  between the coaxial cable core and its guard, the measured current is

$$I_{\text{lift}} = C_P \dot{V} + C_C \dot{V}_C, \quad (\text{A.1})$$

where  $V_C$  is the compensation voltage applied to the guard. We obtain the value for  $C_P$  by measuring  $I_{\text{lift}}$  when applying a known  $\dot{V}$  and keeping  $V_C$  at zero, and similarly for  $C_C$ :

$$C_P = \left. \frac{I_{\text{lift}}}{\dot{V}} \right|_{V_C=0}, \quad (\text{A.2})$$

$$C_C = \left. \frac{I_{\text{lift}}}{\dot{V}_C} \right|_{V=0}. \quad (\text{A.3})$$

Equations (A.2) and (A.3) provide a characterization of the linear transfer function between  $V$  and  $I_{\text{lift}}$  and between  $V_C$  and  $I_{\text{lift}}$ , respectively. Knowing  $C_P$  and  $C_C$  it is trivial to apply a  $V_C$  that exactly cancels the contribution from the parasitic capacitance:

$$V_C(t) = -\frac{C_C}{C_P} V(t). \quad (\text{A.4})$$

Because  $C_P$  includes the capacitive contributions that originate at the millimeter to meter scale (probe holder, cables, and measurement electronics), its value is not changing significantly between the lifted and scanning positions of the AFM tip. The compensation from Eq. (A.4) is therefore constant while scanning.

## 3. Detailed analysis

With proper compensation of the parasitic current  $I_P = C_P V$ , Eq. (1) becomes:

$$I = I_G + I_D = G(V)V + C(V)\dot{V}. \quad (\text{A.5})$$

We apply a time-dependent sample bias of the form

$$V(t) = V_{\text{AC}} \cos(\omega_1 t), \quad (\text{A.6})$$

so that the measured current through the tip becomes

$$I_G(t) = V_{\text{AC}} G[V(t)] \cos(\omega_1 t), \quad (\text{A.7})$$

$$I_D(t) = -\omega_1 V_{\text{AC}} C[V(t)] \sin(\omega_1 t). \quad (\text{A.8})$$

Assuming  $G(V)$  and  $C(V)$  are analytic functions, they share the same time periodicity as  $V$  and can therefore be written as a Fourier series:

$$G(V) = \sum_{m=0}^{+\infty} g_m \cos(m\omega_1 t), \quad (\text{A.9})$$

$$C(V) = \sum_{m=0}^{+\infty} c_m \cos(m\omega_1 t), \quad (\text{A.10})$$

where the  $\{g_m\}$  and  $\{c_m\}$  are real coefficients. The two currents finally become

$$I_G(t) = V_{\text{AC}} \cos(\omega_1 t) \sum_{m=0}^{+\infty} g_m \cos(m\omega_1 t) \\ = \sum_{k=0}^{+\infty} I_{Gk} \cos(k\omega_1 t), \quad (\text{A.11})$$

$$I_D(t) = -\omega_1 V_{\text{AC}} \sin(\omega_1 t) \sum_{m=0}^{+\infty} c_m \cos(m\omega_1 t) \\ = \sum_{k=0}^{+\infty} I_{Dk} \sin(k\omega_1 t), \quad (\text{A.12})$$

where the  $\{I_{Gk}\}$  and  $\{I_{Dk}\}$  are real constants. Equations (A.11) and (A.12) correspond to (2) and (3), and show that the two current contributions are easily distinguishable: the galvanic current is in phase with the cosine (and therefore  $V$ ), and the displacement current is in phase with the sine (and therefore  $\dot{V}$ ). This fact becomes evident by inserting (2) and (3) into (A.5) and taking the Fourier Transform, yielding

$$\hat{I}(\omega) = \sum_{k=0}^{+\infty} \frac{I_{Gk} - iI_{Dk}}{2} \hat{\delta}(\omega - k\omega_1) \\ + \sum_{k=0}^{+\infty} \frac{I_{Gk} + iI_{Dk}}{2} \hat{\delta}(\omega + k\omega_1), \quad (\text{A.13})$$

and therefore Eq. (4) and (5).

#### 4. Symmetry of IVC

An arbitrary curve can be decomposed into an even- and an odd-symmetry curve around zero. For our IVC:

$$I_G(V) = I_{\text{even}}(V) + I_{\text{odd}}(V), \quad (\text{A.14})$$

$$I_{\text{even}}(V) = \frac{1}{2}[I_G(V) + I_G(-V)], \quad (\text{A.15})$$

$$I_{\text{odd}}(V) = \frac{1}{2}[I_G(V) - I_G(-V)]. \quad (\text{A.16})$$

We then quantify the magnitude of each contribution by using the norm

$$\|I\|^2 = \int_{-V_{\text{AC}}}^{V_{\text{AC}}} |I(V)|^2 dV, \quad (\text{A.17})$$

and the symmetry parameter defined as

$$S = \frac{\|I_{\text{even}}\|}{\|I_{\text{even}}\| + \|I_{\text{odd}}\|}. \quad (\text{A.18})$$

$S$  is equal to zero for a purely odd curve, equal to one for a purely even curve, and between zero and one for any other curve.

\* borgani@kth.se

- <sup>1</sup> M. Si, C.-J. Su, C. Jiang, N. J. Conrad, H. Zhou, K. D. Maize, G. Qiu, C.-T. Wu, A. Shakouri, M. A. Alam, and P. D. Ye, *Nature Nanotechnology* **13**, 24 (2018).
- <sup>2</sup> P. Ghamgosar, F. Rigoni, S. You, I. Dobryden, M. G. Kohan, A. L. Pellegrino, I. Concina, N. Almqvist, G. Malandrino, and A. Vomiero, *Nano Energy* **51**, 308 (2018).
- <sup>3</sup> A. Wedig, M. Luebben, D.-Y. Cho, M. Moors, K. Skaja, V. Rana, T. Hasegawa, K. K. Adepalu, B. Yildiz, R. Waser, and I. Valov, *Nature Nanotechnology* **11**, 67 (2015).
- <sup>4</sup> R. Berger, H. J. Butt, M. B. Retschke, and S. A. L. Weber, *Macromolecular Rapid Communications* **30**, 1167 (2009).
- <sup>5</sup> J. Liu, A. Goswami, K. Jiang, F. Khan, S. Kim, R. McGee, Z. Li, Z. Hu, J. Lee, and T. Thundat, *Nature Nanotechnology* **13**, 112 (2018).
- <sup>6</sup> D. C. Coffey, O. G. Reid, D. B. Rodovsky, G. P. Bartholomew, and D. S. Ginger, *Nano Letters* **7**, 738 (2007).
- <sup>7</sup> F. Barati, M. Grossnickle, S. Su, R. K. Lake, V. Aji, and N. M. Gabor, *Nature Nanotechnology* **12**, 1134 (2017).
- <sup>8</sup> G. Otnes and M. T. Borgström, *Nano Today* **12**, 31 (2017).
- <sup>9</sup> R. M. Lutchyn, E. P. A. M. Bakkers, L. P. Kouwenhoven, P. Krogstrup, C. M. Marcus, and Y. Oreg, *Nature Reviews Materials* **3**, 52 (2018).
- <sup>10</sup> Ö. Güll, H. Zhang, J. D. S. Bommer, M. W. A. de Moor, D. Car, S. R. Plissard, E. P. A. M. Bakkers, A. Geresdi, K. Watanabe, T. Taniguchi, and L. P. Kouwenhoven, *Nature Nanotechnology* **13**, 192 (2018).

- <sup>11</sup> J. A. Galvis, E. Herrera, C. Berthod, S. Vieira, I. Guillamón, and H. Suderow, *Communications Physics* **1**, 30 (2018).
- <sup>12</sup> D. Mikulik, M. Ricci, G. Tutuncuoglu, F. Matteini, J. Vukajlović, N. Vulic, E. Alarcon-Llado, and A. Fontcuberta i Morral, *Nano Energy* **41**, 566 (2017).
- <sup>13</sup> S. Somnath, K. J. H. Law, A. N. Morozovska, P. Maksymovych, Y. Kim, X. Lu, M. Alexe, R. Archibald, S. V. Kalinin, S. Jesse, and R. K. Vasudevan, *Nature Communications* **9**, 513 (2018).
- <sup>14</sup> A. Belianinov, S. V. Kalinin, and S. Jesse, *Nature Communications* **6**, 1 (2015).
- <sup>15</sup> H. Kwon, J.-S. Yoon, Y. Lee, D. Y. Kim, C.-K. Baek, and J. K. Kim, *Sensors and Actuators B: Chemical* **255**, 1663 (2018).
- <sup>16</sup> I. Concina, Z. H. Ibupoto, and A. Vomiero, *Advanced Energy Materials* **7**, 1700706 (2017).
- <sup>17</sup> S. Rühle, A. Y. Anderson, H.-N. Barad, B. Kupfer, Y. Bouhadana, E. Rosh-Hodesh, and A. Zaban, *The Journal of Physical Chemistry Letters* **3**, 3755 (2012).
- <sup>18</sup> H.-M. Kim, J. Kim, S.-Y. Cho, and J. Jang, *ACS Applied Materials & Interfaces* **9**, 38678 (2017).
- <sup>19</sup> J. W. Cooley and J. W. Tukey, *Mathematics of Computation* **19**, 297 (1965).
- <sup>20</sup> E. Jones, T. Oliphant, P. Peterson, *et al.*, “SciPy: Open source scientific tools for Python,” (2001–), [online, available at <http://www.scipy.org/>].
- <sup>21</sup> R. Borgani, P.-A. Thorén, D. Forchheimer, I. Dobryden, S. M. Sah, P. M. Claesson, and D. B. Haviland, *Physical Review Applied* **7**, 064018 (2017).